Research Article

Ying Li*, Siren Guo, Yudi Li, Kaiyou Wu, Linlin Zhao, Xi Liu, Xulin Yang, Pan Wang, Yuxin Yang, Yan Sun, and Zihao Mou

Electrostatic-spinning construction of HCNTs@$Ti_3C_2T_x$ MXenes hybrid aerogel microspheres for tunable microwave absorption

https://doi.org/10.1515/rams-2023-0339
received May 03, 2023; accepted July 01, 2023

Abstract: Helical carbon nanotubes (HCNTs) are chiral materials that can form an induced magnetic field when current passes through them, making them a desirable material for absorbing microwaves. However, poor electrical properties and inert surfaces limit the application of HCNTs as sole materials. In this study, we develop HCNTs@$Ti_3C_2T_x$ MXenes hybrid aerogel microspheres synthesized using an electrospinning-assisted ice template method. The modified surfaces of the HCNTs form hydrogen bonds with $Ti_3C_2T_x$ MXenes to produce hybrid aerogel microspheres. Because of the different functionalized surfaces of HCNTs (F-HCNTs), F-HCNTs@$Ti_3C_2T_x$ MXenes could be adjusted to obtain effective reflection loss (RL) of microwaves ranging from 2 to 18 GHz. The observed advantageous RL is attributed to the modified surface of the HCNTs, their porous structure, and the optimized impedance matching derived from the synergistic effect between HCNTs and $Ti_3C_2T_x$ MXenes. Successful assembly method for the 3D architectures of HCNTs@$Ti_3C_2T_x$ MXenes hybrid aerogel microspheres significantly widens the practical applications of HCNTs in microwave absorption.

Keywords: helical carbon nanotubes, $Ti_3C_2T_x$ MXenes, aerogel microspheres, microwave absorption

1 Introduction

Helical carbon nanotubes (HCNTs) have drawn considerable research interest in terms of electromagnetic interference shielding due to their unique chiral features, low density, high theoretical microwave absorption (MA), and multiple attenuating mechanisms [1,2]. Chiral parameters are adjustable and typically cause circular dichroism and optical rotation due to the generation of cross-coupling effects in external alternating electromagnetic fields [3,4]. In addition, the unique chiral feature can arouse cross-polarization and leads to resonance losses in microwave fields, and the carbonaceous nanostructures can induce cross-conductive losses [5–7]. However, the carbonaceous nature leads to high dielectric loss and weak impedance matching. The mainstream strategy used to optimize impedance matching is to construct HCNT-based composites by incorporating with magnetic or dielectric materials, such as cooperating magnetic metals and metal oxides, on the surfaces of helical carbon nanofibers [8,9], or to introduce defects to adjust their dielectric properties [10–12]. However, magnetic metals or metal oxides are dense and readily corrosive, and introducing defects is a laborious process done at the expense of raw materials [13,14].

Constructing 3D porous structures is an ideal approach for adjusting the impedance characteristics of dielectric MA materials. The porous interior has the same characteristics as air, which results in optimized impedance matching with air. With the aid of 2D/1D materials such as graphene and nanofibers used as skeletons, 1D fibers can be used in 3D architectures with high mechanical performance [15–17]. In addition, skeleton materials can form heterointerfaces that cause polarization loss, and their dielectric, electrical, and magnetic properties can optimize the impedance-matching characteristics [18–20]. $Ti_3C_2T_x$ MXenes, which is a flexible 2D material with high theoretical conductivity and active surface properties, has proven to be a potential material for use in electromagnetic protection [21,22], and the rich functional

* **Corresponding author: Ying Li**, School of Mechanical Engineering, Chengdu University, 2025 Chengluo Avenue, Chengdu 610106, China, e-mail: liying@cdu.edu.cn, y.maryli@my.swjtu.edu.cn
Siren Guo, Yudi Li, Kaiyou Wu, Linlin Zhao, Xulin Yang, Pan Wang, Yuxin Yang, Yan Sun, Zihao Mou: School of Mechanical Engineering, Chengdu University, 2025 Chengluo Avenue, Chengdu 610106, China
Xi Liu: School of Automotive Engineering, Chengdu Aeronautic Polytechnic, Chengdu, 610100, China

groups on its surface enable it to be modified with other materials without harming the intrinsic properties or destroying the structures of those materials [23–25]. Based on its active surface character, $Ti_3C_2T_x$ MXenes have been used as a promising dielectric mediator to enhance the MA performance of absorbers [26,27]. Therefore, a 3D hybrid constructed with HCNTs and $Ti_3C_2T_x$ MXenes would take advantage of both 2D and chiral microstructural materials and further improve MA performance due to the enhancement of the dielectric loss capability and optimized impedance matching driven from the newly formed heterointerfaces and pore structures as well as the introduction of $Ti_3C_2T_x$ MXenes as the conductive loss component.

In this article, the construction of novel HCNTs@$Ti_3C_2T_x$ MXenes hybrid aerogel microspheres by integrating HCNTs with $Ti_3C_2T_x$ MXenes through a freeze-drying-assisted electrostatic spinning technique is demonstrated for the first time. Due to the hydrogen bonds between the functional HCNTs (F-HCNTs) and $Ti_3C_2T_x$ MXenes layers, the $Ti_3C_2T_x$ MXenes layers are well assembled with HCNTs to form heterogeneous structures. Molecular dynamic simulations are performed to investigate these interactions. A series of HCNTs@$Ti_3C_2T_x$ MXenes with different interlayer structures are obtained by altering the treatment times of the HCNTs. Accordingly, the structures and MA performances are studied and optimized. Successful assembly methods for the 3D architectures of HCNTs@$Ti_3C_2T_x$ MXenes hybrid aerogel microspheres significantly widen the practical applications of HCNTs in MA.

2 Experimental section

2.1 Preparation of HCNTs and $Ti_3C_2T_x$ MXenes

The original HCNTs (O-HCNTs) were prepared in our laboratory through chemical vapor deposition [28,29]. Before use, the O-HCNTs were annealed (denoted as A-HCNTs) and washed (denoted as H-HCNTs) to remove amorphous carbon and excess precursors. The F-HCNTs were prepared by immersing the H-HCNTs in a mixed acid (HNO_3/H_2SO_4 = 1/3 by volume) at various set times (0.5, 1, 3, and 6 h). The F-HCNTs modified under different times are denoted as F-HCNTs-X h. $Ti_3C_2T_x$ MXenes were prepared based on the method described in the study of Alhabeb *et al.* [30].

2.2 Preparation of HCNTs@$Ti_3C_2T_x$ MXenes aerogel microspheres

Totally, 18 mg of HCNTs and 8.4 mL of water were added to 1.6 mL of the $Ti_3C_2T_x$ MXenes dispersion (5 mg·mL^{-1}) and stirred for 5 min. The mixture was then placed in a polypropylene syringe, and the spinning process was started immediately at a voltage of approximately 5 kV under an injection rate of approximately 0.08 mL·min^{-1}. The ice in the frozen droplets was sublimed in a vacuum freeze dryer for 2 days, and hybrid aerogel microspheres were obtained. These aerogels were stored in a sealed vial at −20°C to avoid oxidization of MXenes.

2.3 Characterization

Scanning electron microscopy (SEM; JEOL JSM-7800F) and transmission electron microscopy (TEM; JEOL JEM-2100) were used to characterize the morphologies. Raman spectra were recorded using a Renishaw InVia Reflex instrument at an excitation wavelength of 532 nm to explore the structure of HCNTs and MXenes. Fourier transform infrared spectroscopy (FT-IR) (Bruker Tensor II) was performed to investigate the structural change of HCNTs after surface treatments. The pore size distribution and specific surface areas were obtained by using conventional nitrogen physisorption measurements (Gold APP V-Sorb 2800P) based on Barrett–Joyner–Halenda (BJH) and Brunauer–Emmett–Teller (BET) methods. The electromagnetic parameters were collected by the coaxial-line method. A vector network analyzer (VNA, Agilent 15071C) was used, and the testing range is 2–18 GHz. The samples were prepared by the same method as the previous work [10].

3 Results and discussion

3.1 Fabrication of HCNTs@MXene

Figure 1a shows the structural evolution of HCNTs and the preparation of HCNTs@MXenes. To form a 3D structure, HCNTs were expected to react with MXenes; thus, a mixed acid was introduced to activate the surfaces [31]. Surface characteristics are crucial not only for constructing 3D structures but also for tuning the MA performance. Of the original

HCNTs, the O-HCNTs presented a mirror-symmetrical morphology with unilateral nanotubes in a kink-like helical shape, which has previously been demonstrated to be favorable to the absorption of microwaves (Figure S1a) [32]. When treated with mixed acid, the morphologies, structures, and properties of HCNTs exhibit remarkable changes [33]. This enables better dispersion in water and cooperation with MXenes due to the grafting of oxygen-containing groups. The MXenes used in this study is a type of large-scale 2D nanoflake (Figure S1b) whose surface contains abundant hydroxyl groups, thus offering a large area to hold HCNTs and form 3D architectures. During mixing, HCNTs and MXenes nanoflakes are homogeneously dispersed in water. During electrospinning, the combined force of electric and gravity fields causes the spinning solution to form a Taylor cone at the needle tip. When the voltage is high enough, this Taylor cone breaks away from the needle tip and is immediately frozen in a liquid nitrogen bath [18]. The particles in the spinning solution containing F-HCNTs and MXenes nanoflakes are concentrated on the ice grain boundaries and squeezed to form 3D networks [34]. Because the temperature gradient is from the surface to the center of the droplet, ice grows directionally, and therefore the spatial distribution of MXenes as determined by the grain boundary is radial [35]. In our study, after the ice was sublimated in a vacuum freeze dryer, aerogel microspheres with directional pores were obtained (Figure S2). The specific surface areas were calculated from N_2 adsorption using the BET method (Figure S3). A 3D network structure of aerogel microspheres consisting of macropores was constructed by HCNTs@MXenes junctions. In addition, the MXenes layers are stacked on each other during the dispersion and freeze-drying process. This method hardly forms micropores and mesopores, as confirmed by the BJH pore size distribution. Therefore, the specific surface area measured through N_2 adsorption is relatively low. The specific surface area of pure MXene aerogel microsphere is 137.6 $m^2 \cdot g^{-1}$, which got remarkable improvement after adding F-HCNTs, such as the specific surface area of F-HCNTs-0.5 h@MXenes is 252.6 $m^2 \cdot g^{-1}$. However, the specific surface area showed a decreasing trend as extending the treating time of F-HCNTs. For F-HCNTs-1.0 h@MXenes, the specific surface area is 248.1 $m^2 \cdot g^{-1}$, F-HCNTs-3.0 h@MXenes is 246.9 $m^2 \cdot g^{-1,}$ and F-HCNTs-6.0 h@MXenes is 208.3 $m^2 \cdot g^{-1}$, indicating that the treatment of mixing acid on HCNTs was favorable to increasing porosity. As mentioned in previous work [33], the morphologies and structures of

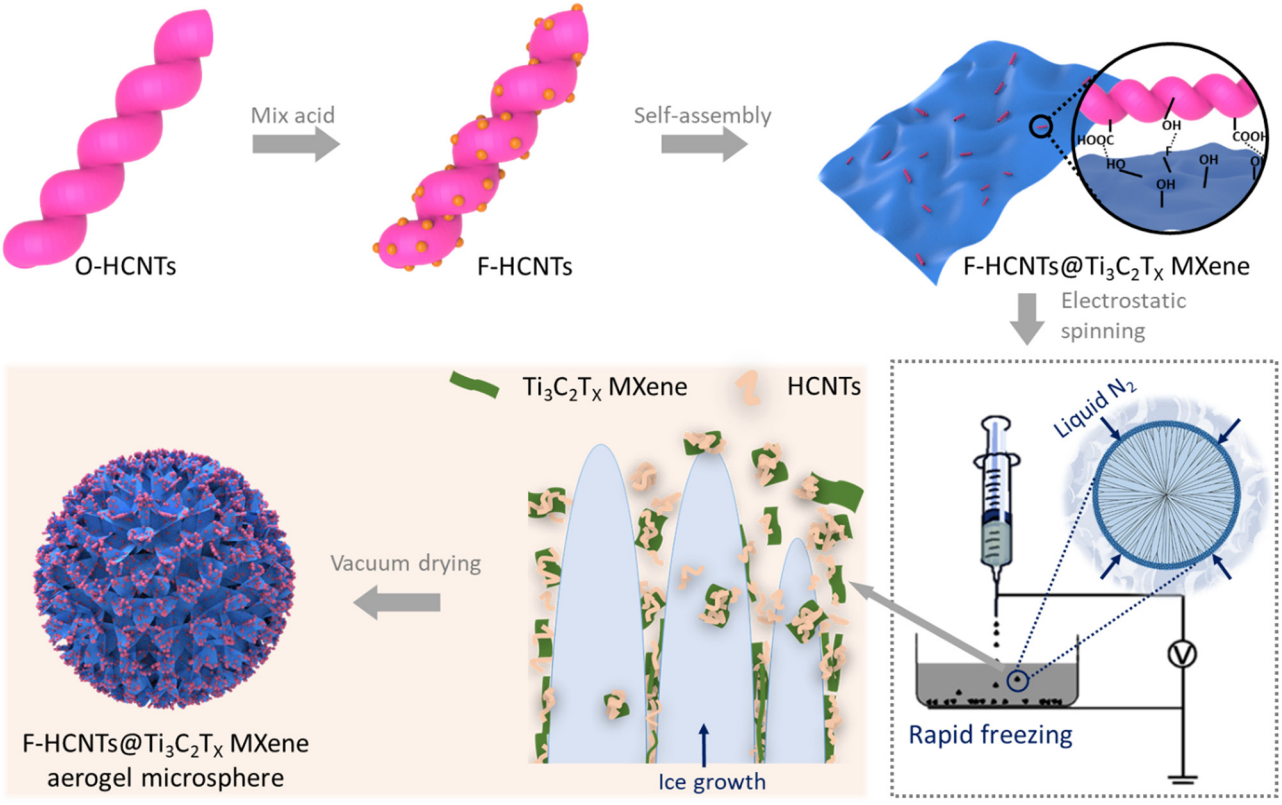

Figure 1: Schematic of preparing HCNTs@$Ti_3C_2T_x$ MXenes hybrid aerogel microspheres.

HCNTs would be destroyed after excessive treatment by mixing acid, resulting in shortened and cut-open nanotubes, which, therefore, causes a decrease in the specific surface area [36].

The obtained aerogel microspheres are presented in Figure 2a–c. Because of the balance force between electric and gravitational fields, the diameters of microdroplets are approximately 800 μm after the droplets exit the needle tip. In addition, the droplets are round, which may be due to comprehensive factors such as uneven liquid nitrogen levels and the vaporization microenvironment [18]. After sublimation, air replaces the ice crystals, and the remaining droplets are porous. The structure of a 3D porous network is significantly affected by the particle properties, which cause entrapment or repulsion by different interaction forces between the particles and solidification fronts [37]. The MXenes flakes are hydrophilic and thus tend to become entrapped by solidification fronts, resulting in curved cell walls inside the HCNTs@MXenes aerogels (Figure 2a′–c′). The oxidation of HCNTs renders them more hydrophilic, which is beneficial in avoiding self-aggregation and binding to MXenes through hydrogen bonding. As the enlarged views show, the HCNTs became more uniformly dispersed on the MXenes flakes as the treatment time increased.

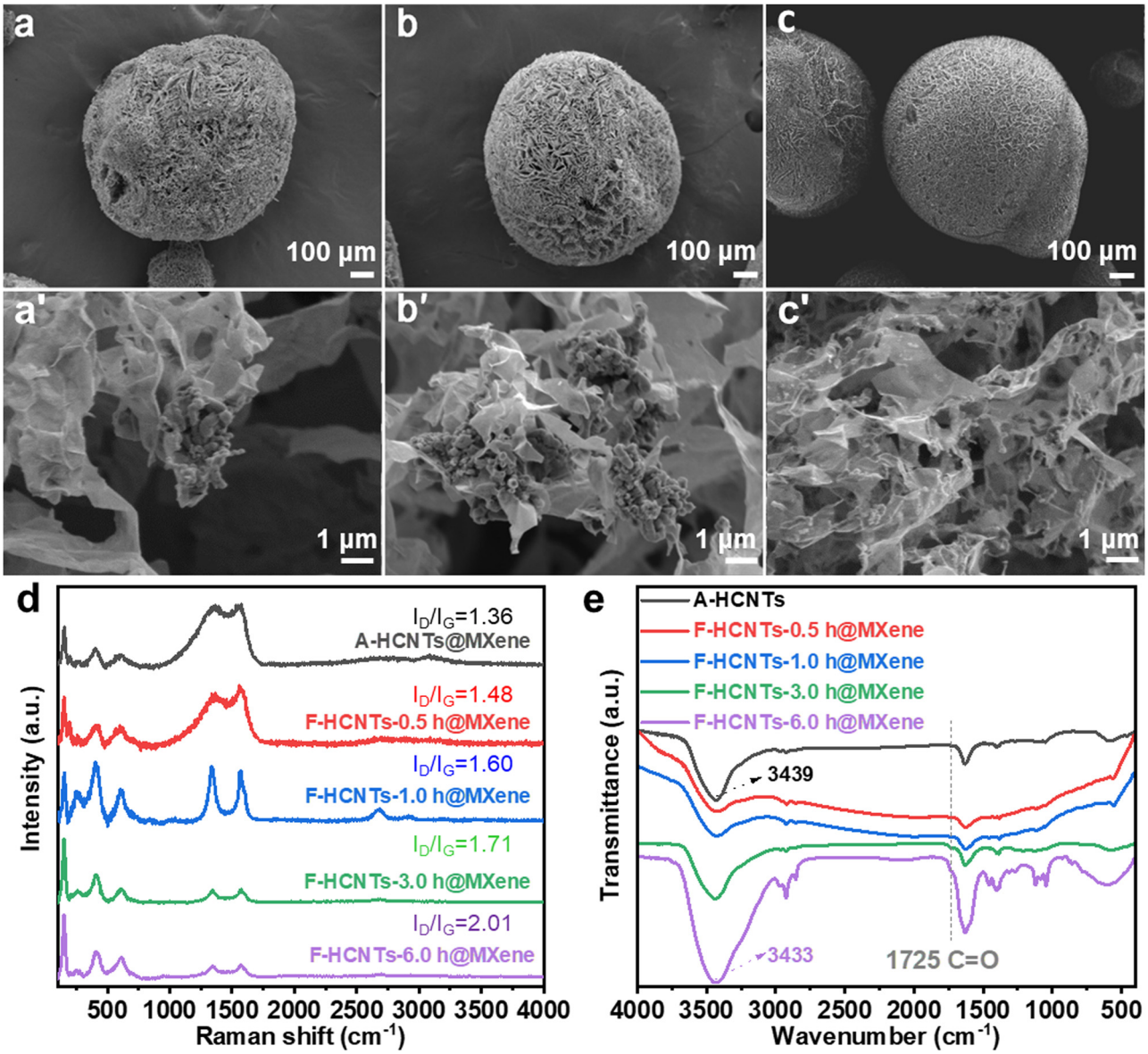

Figure 2: Morphological and structural analysis of HCNTs@MXenes hybrid aerogels. SEM images of (a) A-HCNTs@MXenes, (b) F-HCNTs-1 h@MXenes, and (c) F-HCNTs-6 h@MXenes. (a′)–(c′) provide details of (a)–(c) under a high magnification, respectively. (d) Raman spectra and (e) FT-IR spectra of HCNTs@MXenes.

However, the aggregation of HCNTs could not be completely avoided. As Figure 2a′–c′ shows, HCNT aggregates dispersed on the MXenes skeleton instead of on single tubes. However, the aggregates were dispersed more evenly when the HCNTs were treated for a longer time, which in turn improved the dispersion of the F-HCNTs in water and their interaction with MXenes. The interactions between the HCNTs and MXenes were confirmed by the Raman spectra, where the characteristic peaks of the graphite structure (D and G bands) at 1,349 and 1,586 cm^{-1} [38] and peaks of $Ti_3C_2T_x$ MXenes at approximately 200 and 400 cm^{-1}, respectively, could be found [39] (Figure 2d). More importantly, after integration, the widths of the D and G bands broadened, and the I_D/I_G ratio increased from 1.36 to 2.01, which was much higher than the value after modification by acid mixing [33]. The higher I_D/I_G ratio for the F-HCNTs@MXenes was attributed to the introduction of MXenes, which interacted with the F-HCNTs and caused an increase in disordered carbon in these samples [40]. An improved I_D/I_G ratio implied the formation of more defects, which can serve as polarization centers and improve polarization loss. Figure 2e shows the FT-IR spectra of the F-HCNTs@MXenes. The peak at approximately 1,725 cm^{-1} represents the vibration of C═O in –COOH and demonstrates the successful modification of F-HCNTs. More importantly, the shift of the C–OH vibration bonds from 3,436 to 3,428 cm^{-1} shows the hydrogen bond interactions among F-HCNTs and MXenes [41].

3.2 MA performance

The MA performance of F-HCNTs@MXenes was studied based on the transmission line theory by evaluating the experimental data, which includes the complex permittivity ($\varepsilon = \varepsilon' - j\varepsilon''$) and permeability ($\mu = \mu' - j\mu''$). Electromagnetic parameters (2–18 GHz) were collected by the coaxial-line method on VNA. The real and image parts of $\varepsilon(\varepsilon')$ and $\mu(\mu')$ and their loss tangents (calculated by Eqs. (1) and (2)) of F-HCNTs@MXenes wax composites with different treatment times are shown in Figure 3. Here, ε' represents the dielectric and polarization properties of materials. In addition, the increase of ε' indicates that the material is more susceptible to polarization in the magnetic/electric fields. ε'' represents the dielectric loss ability of materials. In Figure 3a, ε' tends to decrease with increasing frequency, which can be explained by the hysteresis increase of polarization relative to electric-field changes at higher frequencies [42,43]. It is noteworthy that strong resonance peaks of F-HCNTs-0.5 h@MXenes exist over the entire testing frequency range, particularly in the low-frequency band. However, the curves of the other F-HCNTs@MXenes are relatively flat. In addition, the variation law of the ε'' shows a similar rising trend to ε' in the testing frequency range, as shown in Figure 3b. Obviously, multiple resonance peaks exist at 2–18 GHz in the ε'' curves. This phenomenon can be explained in two respects. First, interfacial polarization relaxation occurred at the heterointerfaces and

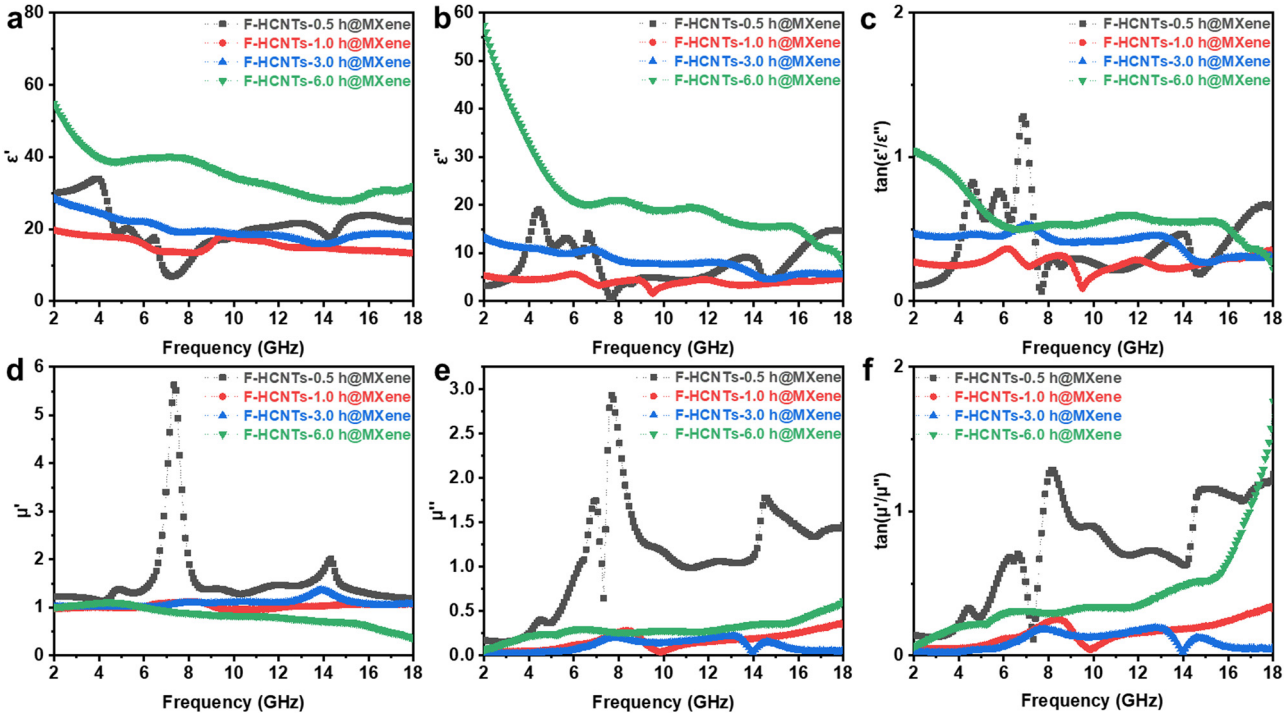

Figure 3: Measured frequency dependence of (a) ε', (b) ε'', (c) tan($\varepsilon'/\varepsilon''$), (d) μ', (e) μ'', and (f) tan(μ'/μ'') of F-HCNTs@MXenes.

junction regions between the HCNTs and $Ti_3C_2T_x$ MXenes. On the other hand, the microwave dissipation ability of absorbers was unstable, resulting in severe fluctuation of the ε'' curves [44,45]. In addition, ε' of F-HCNTs@MXenes increased with an increase in treatment time of the F-HCNTs from 1 to 6 h, which was contrary to the results of the F-HCNTs. The enhanced dielectric and polarization properties of F-HCNTs@MXenes may have benefitted from the improved dispersion of F-HCNTs on MXenes, which also contributed to ε'', indicating that an increase in the treatment time was beneficial to electromagnetic wave loss. The contribution of conductive and polarization loss to dielectric loss can be analyzed and calculated through Debye's theory. As shown in Eq. (3), ε'' can be classified as ε_p'' which is induced by relaxation and ε_c'' which is generated from conductivity, where τ is the relaxation time, σ is the conductivity, and ω is the angular frequency. By fitting with a nonlinear square fitting mode, the contribution of polarization loss and conductive loss can be obtained (see details in the Appendix) [18]. As Figure S4 shows, ε_c'' was generally higher than ε_p'', which can be ascribed to the formation of conductive networks [46]. Thus, ε_c'' plays a key role in dielectric loss. Lightly modified F-HCNTs-0.5 h@MXenes and well-dispersed F-HCNTs-6 h@MXenes showed higher ε_c'' than the others, which was consistent with the previous results.

The tan δ of hybrids is displayed in Figure 3c, demonstrating an obvious dependence on treatment time and implying a remarkable improvement in surface modification and dispersion of F-HCNTs on MXenes to transform electromagnetic energy to other forms [47]. Figure 3d shows a decreasing trend of the μ, and the F-HCNTs-0.5 h@MXenes exhibited the highest capacity in terms of storing and converting electromagnetic energy and had many response peaks in the whole testing range (Figure 3e–f). The magnetic loss capability originated from the catalysts inside the HCNTs. Note that previous studies have shown that ferrite used for catalysis can attenuate electromagnetic energy [5,28]. However, after prolonged treatment with mixed acid, a portion of the catalysis was etched, weakening magnetic loss capability.

$$\tan\ \delta_\varepsilon = \frac{\varepsilon''}{\varepsilon'} = \frac{(\varepsilon_s - \varepsilon_\infty)\omega\tau}{\varepsilon_s + \varepsilon_\infty\omega^2\tau^2}, \tag{1}$$

$$\tan\ \delta_\mu = \frac{\mu''}{\mu'} = \frac{(\mu_s - \mu_\infty)\omega\tau}{\mu_s + \mu_\infty\omega^2\tau^2}, \tag{2}$$

$$\varepsilon''(\omega) = \varepsilon_p'' + \varepsilon_c'' = (\varepsilon_s - \varepsilon_\infty)\frac{\omega\tau}{1 + \omega^2\tau^2} + \frac{\sigma}{\varepsilon_0\omega}. \tag{3}$$

Reflection loss (RL) values that directly reflect the MA performance were calculated using Eqs. (4) and (5), where Z_0 is the impedance of free space, Z_{in} is the impedance of input-characteristic, μ_r and ε_r are the measured complex permeability and permittivity, respectively, d is the thickness of the tested sample, f is the microwave frequency, and c is the speed of light, respectively

$$RL = 20\lg\left|\frac{(Z_{in} - Z_0)}{(Z_{in} + Z_0)}\right|, \tag{4}$$

$$Z_{in} = Z_0\sqrt{\mu_r/\varepsilon_r}\tanh[j(2\pi fd/c\sqrt{\varepsilon_r\mu_r})]. \tag{5}$$

As Figure 4a–b shows, the RL of pristine HCNTs and MXenes is less than −10.0 dB that is the basic requirement of practical use. After integrating them into aerogels, the MA performance can be significantly enhanced. It reached −31.8 dB at 9.7 GHz for the minimal RL (RL_{min}) of F-HCNTs-0.5 h@MXenes with a thickness of 0.7 mm (Figure 4c), and the high MA performance was maintained with increasing thickness. Interestingly, the effective RL shifted to a low-frequency band when the thickness was greater than 3.5 mm, which is desirable for modern MA materials [48]. When the surface treatment time increased to 1 h (Figure 4d), the MA performance decreased slightly. However, as the treatment time increased, the MA capacity shifted to a high-frequency band. For F-HCNTs-3.0 h@MXenes, an RL_{min} of −35.5 dB at 10.6 GHz was reached with a thickness of 2.2 mm, and the effective bandwidth was 2.2 GHz (9.7–11.9 GHz). For F-HCNTs-6.0 h@MXenes, the RL_{min} reached −26.4 dB covering 13.0–16.0 GHz with a thickness of 1.2 mm.

To explain the difference in MA of the F-HCNTs@MXenes, the corresponding parameters were analyzed. The dielectric loss mainly comes from dipole, ion, and electron polarization, where electron and ion polarization were relatively weaker in the microwave range. As mentioned before, the main role of dielectric loss is electric dipole polarization, whose relaxation process can be expressed by Debye dipole relaxation, which is the Cole semicircle:

$$\varepsilon_s = \varepsilon' - j\varepsilon'' = \varepsilon_\infty + \frac{\varepsilon_s - \varepsilon_\infty}{1 + j2\pi f\tau}, \tag{6}$$

where ε_∞ and ε_s are the dielectric constant at the infinite frequency and static dielectric constant, respectively. Thus, ε' and ε'' can be described by

$$\varepsilon' = \varepsilon_\infty + \frac{\varepsilon_s - \varepsilon_\infty}{1 + (j2\pi)^2\tau^2}, \tag{7}$$

$$\varepsilon'' = \frac{2\pi f\tau(\varepsilon_s - \varepsilon_\infty)}{1 + (2f\pi)^2\tau^2}. \tag{8}$$

Then, the relationship between ε' and ε'' can be derived from [49]:

$$\left(\varepsilon' - \frac{\varepsilon_s + \varepsilon_\infty}{2}\right)^2 + (\varepsilon'')^2 = \left(\frac{\varepsilon_s + \varepsilon_\infty}{2}\right)^2. \tag{9}$$

As shown in Eq. (9), the relationship between ε' and ε'' is similar to the equation of circles in the first quadrant, in

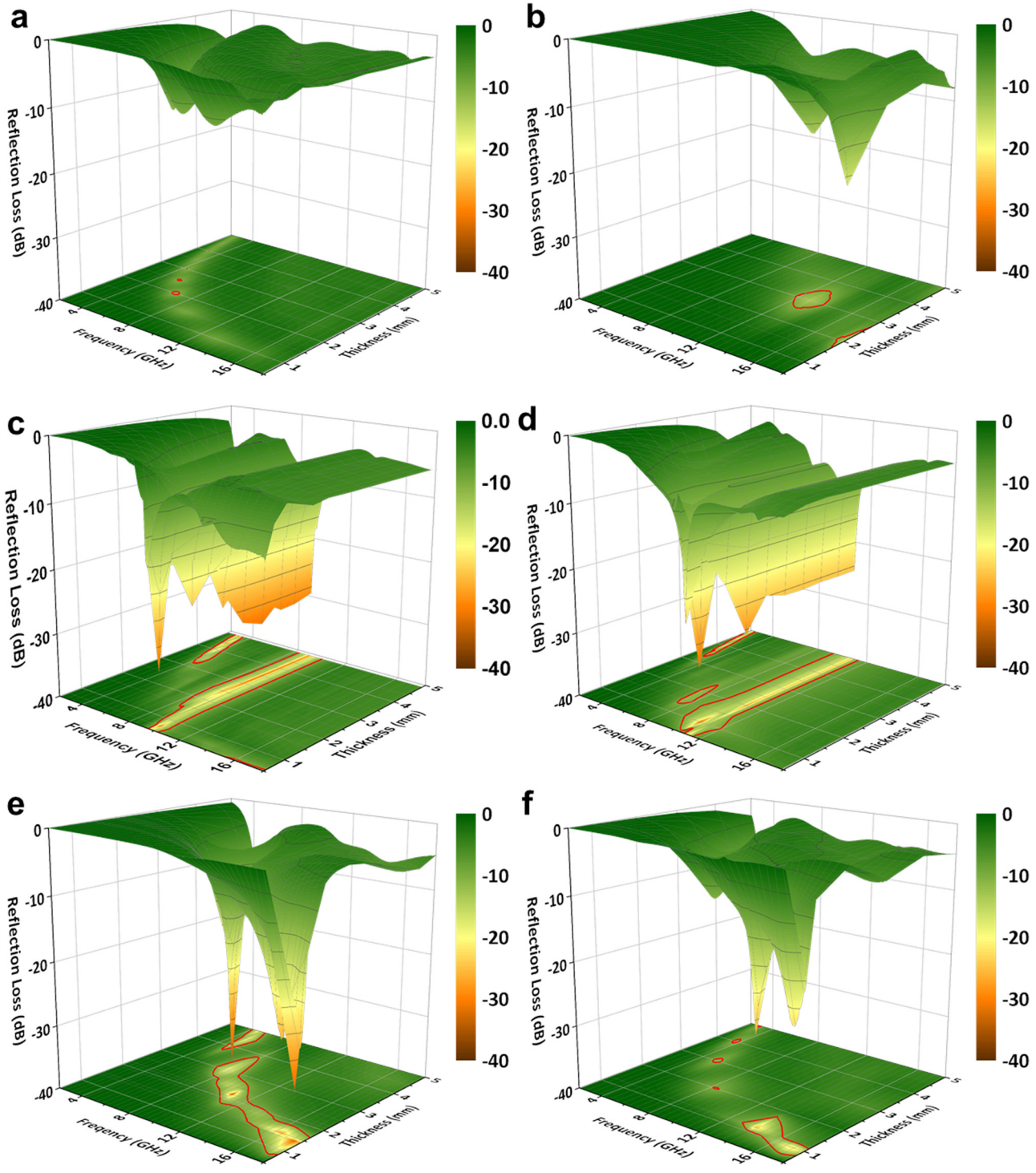

Figure 4: Calculated RL: (a) H-HCNTs, (b) $Ti_3C_2T_x$ MXenes, (c) F-HCNTs-0.5 h@MXenes, (d) F-HCNTs-1.0 h@MXenes, (e) F-HCNTs-3.0 h@MXenes, and (f) F-HCNTs-6.0 h@MXenes.

which each semicircle represents a Debye relaxation process. Figure 5a depicts the semicircles for F-HCNTs@MXenes, indicating the existence of multiple dielectric relaxations. In addition, the radius of semicircles increased as the treatment time increased, which may have derived from an increase in the number of contact interfaces, defects, surface groups, and the amount of conductive loss. The relatively high value of F-HCNTs-0.5 h@MXenes may have

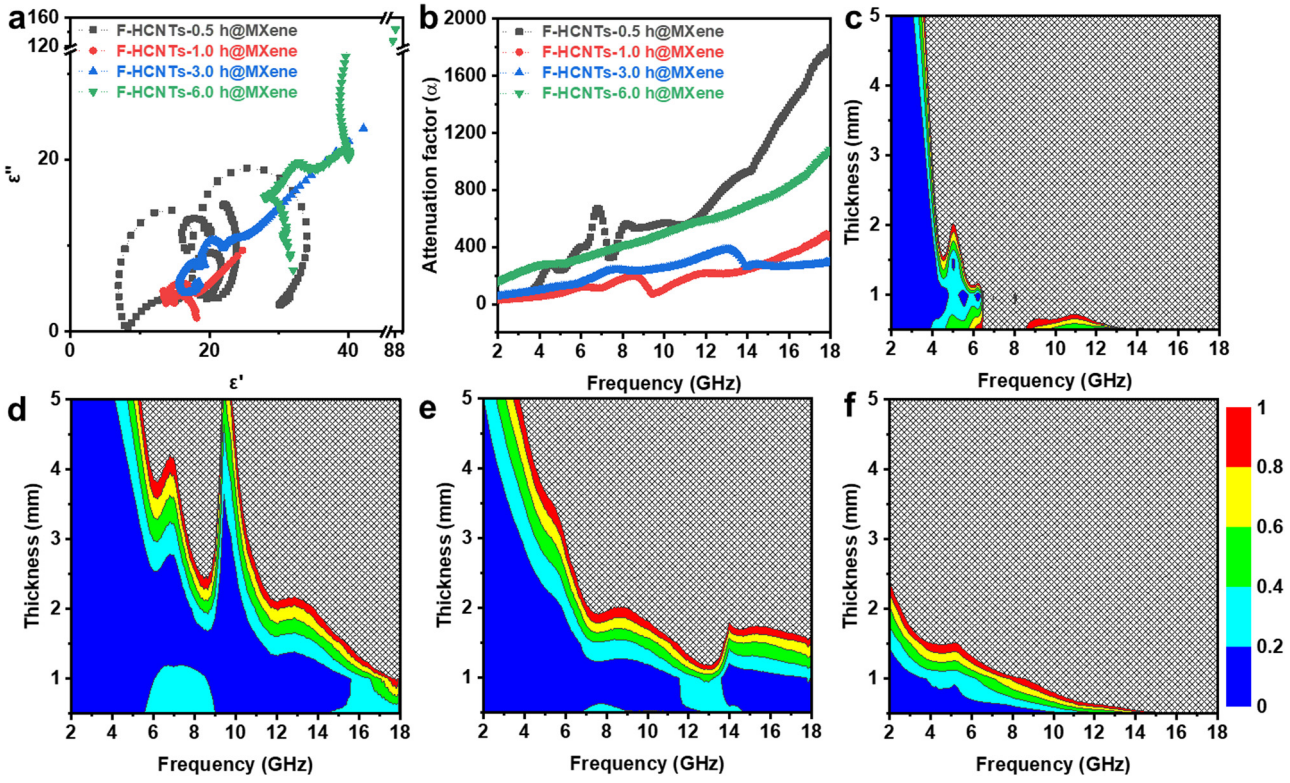

Figure 5: (a) Cole–Cole curves and (b) attenuation factors of F-HCNTs@MXenes, (c)–(f) impedance matching degree of F-HCNTs-0.5 h@MXenes, F-HCNTs-1.0 h@MXenes, F-HCNTs-3.0 h@MXenes and F-HCNTs-6.0 h@MXenes, respectively.

derived from the residual ferrite. Conductivity is also a critical factor affecting the dielectric loss of hybrids, and the existence of a tail in the Cole–Cole curves confirmed the increase in conductive loss derived from the highly conductive $Ti_3C_2T_x$ MXenes. The semicircles indicate the relaxation processes derived from the interfaces between the HCNTs and $Ti_3C_2T_x$ MXenes flakes. Approximately six types of relaxation processes occurred in the hybrids, where a detailed explanation of each semicircle is provided as follows. Only when the material exhibits impedance matching and loss characteristics excellent MA performance can be achieved. To explain the excellent MA performance of F-HCNTs-0.5 h@MXenes, the loss characteristics (attenuation constant α) using Eq. (10) (Figure 5b) were first evaluated, where α showed the same trend as the electric constant, implying that the balance between the residual catalysts and surface groups of HCNTs when adjusted by the treatment time was vital to the microwave loss capability. A more efficient loss characterization may have resulted from the conductive loss. Second, the impedance matching degree (delta Δ) using Eq. (11) was calculated, where M and K can be obtained using Eqs. (12) and (13). An excellent impedance matching degree of MA absorbers should be equal to or close to the impedance matching degree of the free-space interfaces. An excessive impedance matching degree causes reflection, and low impedance matching degree causes transmission of most electromagnetic waves, where a condition of $\Delta < 0.2$ is acceptable [50]. As Figure 5c–f shows, F-HCNTs-1.0 h had the largest area, indicating a superior impedance matching degree, whereas the MA performance was poor due to its low attenuation capability (Figure 5b). The impedance matching degree agreed with the aforementioned RL results, and more importantly, the high impedance matching degree in the S band was the critical factor that endowed the F-HCNTs@MXenes with excellent MA performance in the low-frequency band

$$\alpha = \frac{\sqrt{2}\pi f}{c}\sqrt{(\mu''\varepsilon'' - \mu'\varepsilon') + \sqrt{(\mu''\varepsilon'' - \mu'\varepsilon')^2 + (\mu''\varepsilon'' + \mu'\varepsilon')^2}}, \quad (10)$$

$$\Delta = |\sinh^2(Kfd) - M|, \quad (11)$$

$$K = 4\frac{\pi\sqrt{\mu'\varepsilon'}\sin\left(\frac{\varepsilon+\mu}{2}\right)}{c\cdot\cos\ \varepsilon\cdot\cos\ \mu}, \quad (12)$$

$$M = 4\frac{\mu'\varepsilon'\cos\varepsilon\cdot\cos\ \mu}{(\mu'\cos\varepsilon - \varepsilon'\cos\mu)^2 + \tan^2\left(\frac{\varepsilon-\mu}{2}\right)\cdot(\mu'\cos\varepsilon + \varepsilon'\cos\mu)^2}. \quad (13)$$

In summary, the controllable structural design promotes the controllable MA performance of F-HCNTs@MXenes, which is derived from the impedance matching and

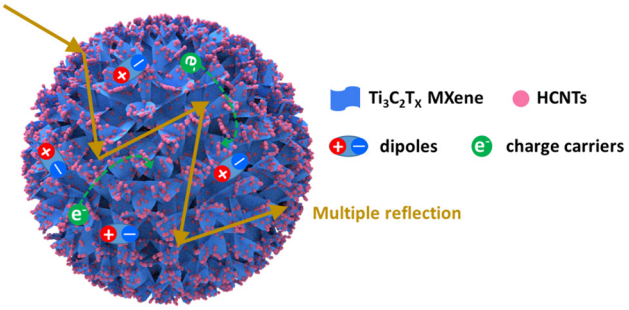

Figure 6: Schematic of the potential MA mechanisms of HCNTs@MXenes.

attenuation constant that are optimized in the process of structural regulation. The surface groups, defects, and conductive loss of both $Ti_3C_2T_x$ MXenes and HCNTs and interfacial polarization between the two components and themselves attribute to the dielectric loss. In addition, the surface modification of HCNTs affected the dielectric loss capability of F-HCNTs@MXenes, which was mainly caused by competition between the residual catalysts, conductive loss, and polarization loss. According to the aforementioned results, a possible MA mechanism for the F-HCNTs@MXenes hybrids is shown in Figure 6: (1) the polarization at interfaces derived from the moving velocities of different induced charges on $Ti_3C_2T_x$ MXenes and HCNTs; (2) the polarization loss resulting from the dipoles of heterointerfaces, defects, amorphous carbon, TiO_2, and surface groups; (3) the conductive loss derived from the HCNTs and $Ti_3C_2T_x$ MXenes flakes; and (4) the pores that optimize the impedance matching and elongate the multiple reflection and scattering.

4 Conclusion

In this study, novel functional HCNTs@$Ti_3C_2T_x$ MXenes hybrid aerogel microspheres for MA were demonstrated. The study showed that through surface modification, active F-HCNTs could interact with $Ti_3C_2T_x$ MXenes and form a 3D porous architecture based on the ice template method. The heterointerface formed by the F-HCNTs and $Ti_3C_2T_x$ MXenes, the porosity of the 3D structure, and the composition of the two materials led to adjustable MA performance. The RL_{min} value reached −35.5 dB at 10.6 GHz was reached with a thickness of 2.2 mm, and the effective bandwidth was 2.2 GHz (9.7–11.9 GHz). These hybrid aerogel microspheres also exhibited excellent MA performance in the S band when the loading of MXenes was tuned. The successful assembly of these hybrids expands the absorption band of HCNT-based materials for both the C–Ku and S bands. Thus, it has the potential to serve as microwave absorbers for army, satellite, and daily protection applications.

Acknowledgments: The authors thank the Ying's Group staff members who supported the processes necessary to carry out the project. In addition, they thank the anonymous reviewers for their fruitful suggestions to improve the article.

Funding information: This work was financially supported by the National Natural Science Foundation of China (No. 52202083), the Science and Technology Planning Project of Longquanyi, Chengdu (No. LQXKJ-KJXM-2022-04), the Natural Science Foundation of Sichuan Province (2022NSFSC0321 and 2022NSFSC0346), and the 2022 Natural Scientific Research Project of Chengdu Aeronautic Polytechnic (No. 06221025).

Author contributions: Conceptualization, methodology, validation, formal analysis, investigation, resources, data curation, writing – original draft preparation, writing – review and editing, visualization, supervision: Ying Li, Siren Guo, Yudi Li, Kaiyou Wu Linlin Zhao, Xi Liu, Pan Wang, Yuxin Yang and Yan Sun; project administration and funding acquisition: Ying Li, Xi Liu, Xulin Yang and Zihao Mou. All authors have accepted responsibility for the entire content of this manuscript and approved its submission.

Conflict of interest: The authors state no conflict of interest.

References

[1] Wang, D.-C., Y. Lei, W. Jiao, Y.-F. Liu, C.-H. Mu, and X. Jian. A review of helical carbon materials structure, synthesis and applications. *Rare Metals*, Vol. 40, No. 1, 2020, pp. 3–19.

[2] Wu, N., Q. Hu, R. Wei, X. Mai, N. Naik, D. Pan, et al. Review on the electromagnetic interference shielding properties of carbon based materials and their novel composites: Recent progress, challenges and prospects. *Carbon*, Vol. 176, 2021, pp. 88–105.

[3] Chen, X., H. Liu, D. Hu, H. Liu, and W. Ma. Recent advances in carbon nanotubes-based microwave absorbing composites. *Ceramics International*, Vol. 4717, 2021, pp. 23749–23761.

[4] Zhao, Y., H. Zhang, X. Yang, H. Huang, G. Zhao, T. Cong, et al. In situ construction of hierarchical core–shell Fe3O4@C nanoparticle-s–helical carbon nanocoil hybrid composites for highly efficient electromagnetic wave absorption. *Carbon*, Vol. 171, 2021, pp. 395–408.

[5] Tian, X., F. Meng, F. Meng, X. Chen, Y. Guo, Y. Wang, et al. Synergistic enhancement of microwave absorption using hybridized polyaniline@helical CNTs with dual chirality. *ACS Applied Materials & Interfaces*, Vol. 9, No. 18, 2017, pp. 15711–15718.

[6] Huang, L., Y. Duan, Y. Shi, X. Ma, H. Pang, Q. Zeng, et al. Chiral asymmetric polarizations generated by bioinspired helical carbon fibers to induce broadband microwave absorption and

multispectral photonic manipulation. *Advanced Optical Materials*, Vol. 1011, 2022, id. 2200249.

[7] Barathi Dassan, E. G., A. Anjang Ab Rahman, M. S. Z. Abidin, and H. M. Akil. Carbon nanotube–reinforced polymer composite for electromagnetic interference application: A review. *Nanotechnology Reviews*, Vol. 9, No. 1, 2020, pp. 768–788.

[8] Tang, H., X. Jian, B. Wu, S. Liu, Z. Jiang, X. Chen, et al. Fe3C/helical carbon nanotube hybrid: Facile synthesis and spin-induced enhancement in microwave-absorbing properties. *Composites Part B: Engineering*, Vol. 107, 2016, pp. 51–58.

[9] Dong, M., M. Peng, W. Wei, H. Xu, C. Liu, and C. Shen. Improved microwave absorption performance of double helical C/Co@CNT nanocomposite with hierarchical structures. *Journal of Materials Chemistry C*, Vol. 9, No. 6, 2021, pp. 2178–2189.

[10] Tao, J., Z. Jiao, L. Xu, P. Yi, Z. Yao, F. Yang, et al. Construction of MOF-Derived Co/C shell on carbon fiber surface to enhance multi-polarization effect towards efficient broadband electromagnetic wave absorption. *Carbon*, Vol. 184, 2021, pp. 571–582.

[11] Zhang, X., Y. Hao, and W. Zhong. Boron-doped helical carbon nanotubes: lightweight and efficient microwave absorbers. *Journal of Materials Science: Materials in Electronics*, Vol. 32, No. 21, 2021, pp. 26161–26172.

[12] Liu, Q., L. Tang, J. Li, Y. Chen, Z. Xu, J. Li, et al. Multifunctional aramid nanofibers reinforced RGO aerogels integrated with high-efficiency microwave absorption, sound absorption and heat insulation performance. *Journal of Materials Science & Technology*, Vol. 130, 2022, pp. 166–175.

[13] Wu, F., K. Yang, Q. Li, T. Shah, M. Ahmad, Q. Zhang, et al. Biomass-derived 3D magnetic porous carbon fibers with a helical/chiral structure toward superior microwave absorption. *Carbon*, Vol. 173, 2021, pp. 918–931.

[14] Zhao, Y., X. Zuo, Y. Guo, H. Huang, H. Zhang, T. Wang, et al. Structural engineering of hierarchical aerogels comprised of multi-dimensional gradient carbon nanoarchitectures for highly efficient microwave absorption. *Nano-micro Letters*, Vol. 13, No. 1, 2021, id. 144.

[15] Han, J., J. Yang, W. Gao, and H. Bai. Ice-templated, large-area silver nanowire pattern for flexible transparent electrode. *Advanced Functional Materials*, Vol. 31, No. 16, 2021, id. 2010155.

[16] Chhetri, K., S. Subedi, A. Muthurasu, T. H. Ko, B. Dahal, and H. Y. Kim. A review on nanofiber reinforced aerogels for energy storage and conversion applications. *Journal of Energy Storage*, Vol. 46, 2022, id. 103927.

[17] Iqbal, A., T. Hassan, Z. Gao, F. Shahzad, and C. M. Koo. MXene-incorporated 1D/2D nano-carbons for electromagnetic shielding: A review. *Carbon*, Vol. 203, 2023, pp. 542–560.

[18] Li, Y., F. Meng, Y. Mei, H. Wang, Y. Guo, Y. Wang, et al. Electrospun generation of Ti3C2Tx MXene@graphene oxide hybrid aerogel microspheres for tunable high-performance microwave absorption. *Chemical Engineering Journal*, Vol. 391, 2020, id. 123512.

[19] Zhao, X., J. Yan, Y. Huang, X. Liu, L. Ding, M. Zong, et al. Magnetic porous CoNi@C derived from bamboo fiber combined with metal-organic-framework for enhanced electromagnetic wave absorption. *Journal of Colloid and Interface Science*, Vol. 595, 2021, pp. 78–87.

[20] Wu, F., Z. Liu, T. Xiu, B. Zhu, I. Khan, P. Liu, et al. Fabrication of ultralight helical porous carbon fibers with CNTs-confined Ni nanoparticles for enhanced microwave absorption. *Composites Part B: Engineering*, Vol. 215, 2021, id. 108814.

[21] Cao, M.-S., Y.-Z. Cai, P. He, J.-C. Shu, W.-Q. Cao, and J. Yuan. 2D MXenes: Electromagnetic property for microwave absorption and electromagnetic interference shielding. *Chemical Engineering Journal*, Vol. 359, 2019, pp. 1265–1302.

[22] Guan, X., Z. Yang, M. Zhou, L. Yang, R. Peymanfar, B. Aslibeiki, et al. 2D MXene Nanomaterials: Synthesis, Mechanism, and Multifunctional Applications in Microwave Absorption. *Small Structures*, Vol. 310, 2022, id. 2200102.

[23] Couly, C., M. Alhabeb, K. L. Van Aken, N. Kurra, L. Gomes, A. M. Navarro-Suárez, et al. Asymmetric flexible mxene-reduced graphene oxide micro-supercapacitor. *Advanced Electronic Materials*, Vol. 4, No. 1, 2018, id. 1700339.

[24] Si, Y., L. Wang, X. Wang, N. Tang, J. Yu, and B. Ding. Ultrahigh-water-content, superelastic, and shape-memory nanofiber-assembled hydrogels exhibiting pressure-responsive conductivity. *Advanced Materials*, Vol. 29, No. 24, 2017, id. 1700339.

[25] Mou, Z. H., R. X. Yan, J. Peng, Y. Li, Z. Y. Huang, Z. J. Wang, et al. Synthesis of polyzwitterionic carbon dots with superior friction and fatigue control behaviors under water lubrication. *Chemical Engineering Journal*, Vol. 465, 2023, id. 142986.

[26] Zhao, S., H. B. Zhang, J. Q. Luo, Q. W. Wang, B. Xu, S. Hong, et al. Highly electrically conductive three-dimensional Ti3C2Tx MXene/reduced graphene oxide hybrid aerogels with excellent electromagnetic interference shielding performances. *ACS Nano*, Vol. 1211, 2018, pp. 11193–11202.

[27] Li, X., X. Yin, C. Song, M. Han, H. Xu, W. Duan, et al. Self-assembly core-shell graphene-bridged hollow MXenes spheres 3D foam with ultrahigh specific EM absorption performance. *Advanced Functional Materials*, Vol. 28, No. 41, 2018, id. 1803938.

[28] Meng, F., Y. Wang, Q. Wang, X. Xu, M. Jiang, X. Zhou, et al. High-purity helical carbon nanotubes by trace-water-assisted chemical vapor deposition: Large-scale synthesis and growth mechanism. *Nano Research*, Vol. 11, No. 6, 2018, pp. 3327–3339.

[29] Chen, X., Y. Li, Y. Wang, D. Song, Z. Zhou, and D. Hui. An approach to effectively improve the interfacial bonding of nano-perfused composites by in situ growth of CNTs. *Nanotechnology Reviews*, Vol. 10, No. 1, 2021, pp. 282–291.

[30] Alhabeb, M., K. Maleski, B. Anasori, P. Lelyukh, L. Clark, S. Sin, et al. Guidelines for synthesis and processing of two-dimensional titanium carbide (Ti3C2Tx MXene). *Chemistry of Materials*, Vol. 29, No. 18, 2017, pp. 7633–7644.

[31] Zhang, Y., Z. Shi, Z. Gu, and S. Iijima. Structure modification of single-wall carbon nanotubes. *Carbon*, Vol. 3815, 2000, pp. 2055–2059.

[32] Feng, J., Y. Wang, Y. Hou, J. Li, and L. Li. Synthesis and microwave absorption properties of coiled carbon nanotubes/CoFe2O4 composites. *Ceramics International*, Vol. 4215, 2016, pp. 17814–17821.

[33] Li, Y., Z. Xu, A. Jia, X. Yang, W. Feng, P. Wang, et al. Controllable modification of helical carbon nanotubes for high-performance microwave absorption. *Nanotechnology Reviews*, Vol. 10, No. 1, 2021, pp. 671–679.

[34] Qiu, L., J. Z. Liu, S. L. Chang, Y. Wu, and D. Li. Biomimetic superelastic graphene-based cellular monoliths. *Nature Communication*, Vol. 3, 2012, id. 1241.

[35] Bouville, F., E. Maire, and S. Deville. Self-assembly of faceted particles triggered by a moving ice front. *Langmuir*, Vol. 30, No. 29, 2014, pp. 8656–63.

[36] Chen, M., H.-W. Yu, J.-H. Chen, and H.-S. Koo. Effect of purification treatment on adsorption characteristics of carbon nanotubes. *Diamond and Related Materials*, Vol. 16, No. 4–7, 2007, pp. 1110–1115.

[37] Körber, C., G. Rau, M. D. Cosman, and E. G. Cravalho. Interaction of particles and a moving ice-liquid interface. *Journal of Crystal Growth*, Vol. 72, No. 3, 1985, pp. 649–662.
[38] Hembram, K., J. G. Kim, S. G. Lee, J. Park, and J. K. Lee. Radial-tangential mode of single-wall carbon nanotubes manifested by Landau regulation: Reinterpretation of low- and intermediate-frequency Raman signals. *Scientific Reports*, Vol. 13, No. 1, 2023, id. 5012.
[39] Sarycheva, A., M. Shanmugasundaram, A. Krayev, and Y. Gogotsi. Tip-enhanced Raman scattering imaging of single- to few-layer Ti(3)C(2)T(x) MXene. *ACS Nano*, Vol. 16, No. 4, 2022, pp. 6858–6865.
[40] Li, B., Z. Ma, J. Xu, X. Zhang, Y. Chen, and C. Zhu. Regulation of impedance matching and dielectric loss properties of N-doped carbon hollow nanospheres modified with atomically dispersed cobalt sites for microwave energy attenuation. *Small*, Vol. 19, No. 28, 2023, id. e2301226.
[41] Fu, Z. Z., S. J. Guo, C. X. Li, K. Wang, Q. Zhang, and Q. Fu. Hydrogen-bond-dominated mechanical stretchability in PVA films: From phenomenological to numerical insights. *Physical Chemistry Chemical Physics*, Vol. 24, No. 3, 2022, pp. 1885–1895.
[42] Quan, B., X. Liang, G. Ji, J. Ma, P. Ouyang, H. Gong, et al. Strong electromagnetic wave response derived from the construction of dielectric/magnetic media heterostructure and multiple interfaces. *ACS Appl Mater Interfaces*, Vol. 911, 2017, pp. 9964–9974.
[43] Smyth, C. P. *Dielectric behavior and structure*, McGraw-Hill Book Co., Inc., New York, 1955.
[44] Tian, W., X. Zhang, Y. Guo, C. Mu, P. Zhou, L. Yin, et al. Hybrid silica-carbon bilayers anchoring on FeSiAl surface with bifunctions of enhanced anti-corrosion and microwave absorption. *Carbon*, Vol. 173, 2021, pp. 185–193.
[45] Tian, Y., D. Zhi, T. Li, J. Li, J. Li, Z. Xu, et al. Graphene-based aerogel microspheres with annual ring-like structures for broadband electromagnetic attenuation. *Chemical Engineering Journal*, Vol. 464, 2023, id. 142644.
[46] Li, T., J. Li, Z. Xu, Y. Tian, J. Li, J. Du, et al. Electromagnetic response of multistage-helical nano-micro conducting polymer structures and their enhanced attenuation mechanism of multi-scale-chiral synergistic effect. *Small*, Vol. 19, No. 21, 2023, id. e2300233.
[47] Sun, H., R. Che, X. You, Y. Jiang, Z. Yang, J. Deng, et al. Cross-stacking aligned carbon-nanotube films to tune microwave absorption frequencies and increase absorption intensities. *Advanced Materials*, Vol. 26, No. 48, 2014, pp. 8120–8125.
[48] Lv, H., Z. Yang, P. L. Wang, G. Ji, J. Song, L. Zheng, et al. A voltage-boosting strategy enabling a low-frequency, flexible electromagnetic wave absorption device. *Advanced Materials*, Vol. 30, No. 15, 2018, id. e1706343.
[49] Xu, H., X. Yin, M. Li, F. Ye, M. Han, Z. Hou, et al. Mesoporous carbon hollow microspheres with red blood cell like morphology for efficient microwave absorption at elevated temperature. *Carbon*, Vol. 132, 2018, pp. 343–351.
[50] Ma, Z., C.-T. Cao, Q.-F. Liu, and J.-B. Wang. A new method to calculate the degree of electromagnetic impedance matching in one-layer microwave absorbers. *Chinese Physics Letters*, Vol. 29, No. 3, 2012, id. 038401.